

JGR Atmospheres

RESEARCH ARTICLE

10.1029/2018JD029630

Key Points:

- Micrometeorological observations during the total solar eclipse of 2017 in soybean, prairie, and forest ecosystems were compared
- Strong eclipse signals were observed for radiation and energy fluxes, although the soybean field experienced convective activity
- Although the eclipse imparted large forcings on surface energy balances, the air temperature response was relatively muted (≤ 2.5 °C)

Supporting Information:

- Supporting Information S1

Correspondence to:

J. D. Wood,
woodjd@missouri.edu

Citation:

Wood, J. D., Sadler, E. J., Fox, N. I., Greer, S. T., Gu, L., Guinan, P. E., et al. (2019). Land-atmosphere responses to a total solar eclipse in three ecosystems with contrasting structure and physiology. *Journal of Geophysical Research: Atmospheres*, 124, 530–543. <https://doi.org/10.1029/2018JD029630>

Received 9 SEP 2018

Accepted 21 DEC 2018

Accepted article online 2 JAN 2019

Published online 18 JAN 2019

Land-Atmosphere Responses to a Total Solar Eclipse in Three Ecosystems With Contrasting Structure and Physiology

J. D. Wood¹ , E. J. Sadler², N. I. Fox¹ , S. T. Greer¹, L. Gu³ , P. E. Guinan¹, A. R. Lupo¹, P. S. Market¹ , S. M. Rochette⁴, A. Speck⁵, and L. D. White⁶ 

¹School of Natural Resources, University of Missouri, Columbia, Missouri, USA, ²Cropping Systems and Water Quality Research Unit, USDA-ARS, Columbia, Missouri, USA, ³Environmental Sciences Division and Climate Change Institute, Oak Ridge National Laboratory, Oak Ridge, Tennessee, USA, ⁴Department of Earth Sciences, The College at Brockport, State University of New York, Brockport, New York, USA, ⁵Department of Physics and Astronomy, University of Missouri, Columbia, Missouri, USA, ⁶Department of Chemistry, Physics, and Atmospheric Science, Jackson State University, Jackson, Mississippi, USA

Abstract Mid-Missouri experienced up to 2 min 40 s of totality at around solar noon during the total eclipse of 2017. We conducted the Mid-Missouri Eclipse Meteorology Experiment to examine land-atmosphere interactions during the eclipse. Here, research examining the eclipse responses in three contrasting ecosystems (forest, prairie, and soybeans) is described. There was variable cloudiness around first and fourth contacts (i.e., the start and end of partial solar obscuration) at the forest and prairie; however, solar irradiance (K_t) signals during the eclipse were relatively clean. Unfortunately, the eclipse forcing at the soybean field was contaminated by convective activity, which decreased K_t beginning about an hour before first contact and exposed the field to cold outflow ~ 30 min before second contact. Turbulence was suppressed during the eclipse at all sites; however, there was also an amplified signal at the soybean field during the passage of a gust front. The standard deviations of the horizontal and vertical wind velocities and friction velocities decreased by $\sim 75\%$ at the forest (aerodynamically rough), and $\sim 60\%$ at the prairie (aerodynamically smooth). The eddy fluxes of energy were highly coherent with the solar forcing with the latent and sensible heat fluxes approaching 0 W/m^2 and changing in direction, respectively. For the prairie site, we estimated a canopy-scale time constant for the surface conductance light response of 10 min. Although the eclipse imparted large forcings on surface energy balances, the air temperature response was relatively muted ($1.5\text{--}2.5$ °C decrease) due to the absence of topographic effects and the relatively moist land and atmosphere.

1. Introduction

Solar eclipses offer the rare opportunity for probing meteorological responses to a forcing of known magnitude and duration (Harrison & Hanna, 2016). The rapid variations in solar radiation affect ecosystem processes and land-atmosphere interactions that have important consequences on the dynamics of the planetary boundary layer. Most investigations of eclipse meteorology have documented variations in atmospheric state variables and winds, with observed responses subject to local conditions that include, but are not limited to, land moisture status (i.e., arid versus moist), geographic location (e.g., maritime versus continental), orography and synoptic or mesoscale conditions (i.e., cloudy versus clear, or being near a frontal boundary), and eclipse magnitude and timing (Anderson, 1999; Aplin et al., 2016; Burt, 2018; Gerasopoulos et al., 2008). In the few micrometeorological studies, common observations include decreased turbulent mixing in the surface layer, rapid variations in sensible (H) and latent (LE) heat fluxes with the former showing a faster and larger response (and a possible change in direction) that is more in phase with solar radiation, and concomitant with stable atmospheric stratification during partial (Antonia et al., 1979; Eaton et al., 1997; Mauder et al., 2007; Stewart & Rouse, 1974; Turner et al., 2018) or total (Foken et al., 2001) eclipse maxima. Of these studies, only Stewart and Rouse (1974) compared multiple ecosystems—a lake, lowland swamp, and upland ridge on the coast of Hudson Bay, Canada. To our knowledge, there has not been a multisite campaign directed to the study of total eclipse micrometeorology above multiple important terrestrial ecosystems within a continental region. We conducted the Mid-Missouri Eclipse Meteorology Experiment during August 2017, of which one component involved the comparison of

Table 1
The Timing of the Phases of Partial and Total Eclipse and the Approximate Length of Totality at the Three Study Sites

	Eclipse Timing (CST)					Duration
	First Contact	Second Contact	Maximum	Third Contact	Fourth Contact	
Forest	10:46:00	12:12:50	12:14:09	12:15:29	13:40:47	2 min 39 s
Prairie	10:46:21	12:13:10	12:14:22	12:15:35	13:40:49	2 min 26 s
Soybean	10:46:01	12:13:04	12:13:50	12:14:36	13:40:10	1 min 32 s

Note that all times are provide in Central Standard Time (CST = UT – 6 hr). At totality, the solar zenith angle at all of the sites was $\sim 27^\circ$.

micrometeorological responses among forest, prairie, and cropland vegetation types—and is the focus of this research reported here. Mid-Missouri was an ideal location for studying eclipse meteorology because the timing was roughly coincident with solar noon (Table 1, Figure S1), and thus far from the morning and afternoon transition periods.

The micrometeorological component of Mid-Missouri Eclipse Meteorology Experiment involved observations at three eddy flux tower sites situated in cropland, prairie, and forest ecosystems. Croplands, forest (and woodland), and prairie (shrubland and grassland) are important land cover types in Missouri, covering 53.7%, 37.6%, and 1.7% of the land area, respectively (USGS National Gap Analysis Program data; https://gis1.usgs.gov/csas/gap/viewer/land_cover/Map.aspx). In this present case, the cropland site was planted with soybeans. These three ecosystem types represent both structural and physiological gradients. Canopy complexity and height (forest > prairie > soybean), vegetation diversity (prairie > forest > soybean), and ecosystem physiology differ across ecosystems.

The overall goal of this research was to examine differences in eclipse micrometeorology over ecosystems defined by contrasting structure and physiology. The specific objectives of this research were to examine variations in (i) atmospheric state variables; (ii) fluxes of radiation, and latent (LE) and sensible (H) heat; and (iii) turbulence and atmospheric stability; and (iv) ecosystem-scale physiological function.

2. Materials and Methods

2.1. Site Descriptions

Eddy covariance (EC) flux tower observations were made in three contrasting ecosystems—forest, prairie, and croplands. At each site, an eddy covariance system consisting of a sonic-anemometer-thermometer and an infrared gas analyzer was deployed above the canopy, to permit the simultaneous measurement of H and LE fluxes. All EC systems sampled at 10 Hz. Supporting meteorological variables (e.g., radiation components, air temperature, and humidity) were also sampled and data recorded at 5-s intervals during the weeks flanking the eclipse—a higher sampling rate than the 30-min averages that are typically recorded for supporting meteorological observations.

All three sites were located within 35 km of Columbia, MO, were separated by a maximum distance of ~ 55 km, and were within the path of totality (Figure 1). The timing of different phases of the eclipse were within 1 min among sites, and the length of totality ranged from 1 min 32 s to 2 min 39 s across sites (Table 1). At the time of the eclipse, the mid-Missouri ecosystems studied here were drought-free according to the U.S. Drought Monitor (Figure S2) and predawn leaf water potential measurements at the forest site ($\Psi_{pd} \approx -0.35$ MPa).

2.1.1. Forest

The Missouri Ozarks AmeriFlux site (MOFLUX, site-id US-MOz; latitude 38.7441, longitude -92.2001) is located ~ 30 km south of Columbia MO at the University of Missouri's Baskett Wildlife Research and Education Center. The second-growth upland oak-hickory forest is approximately 90 years in age. The mean tree height of the top quartile is ~ 22 m (Gu, Pallardy, Yang, et al., 2016), and the mean canopy height ranges from 17 to 20 m throughout the forest (Yang et al., 2007). Sensors are deployed on a 32-m walk-up scaffold tower that was established in 2004. For a more complete description of the MOFLUX forest and micrometeorological instrumentation, the reader is referred to the literature (Gu et al., 2015; Gu, Pallardy, Hosman, & Sun, 2016; Gu, Pallardy, Yang, et al., 2016; Wood et al., 2018; Yang et al., 2007, 2010).

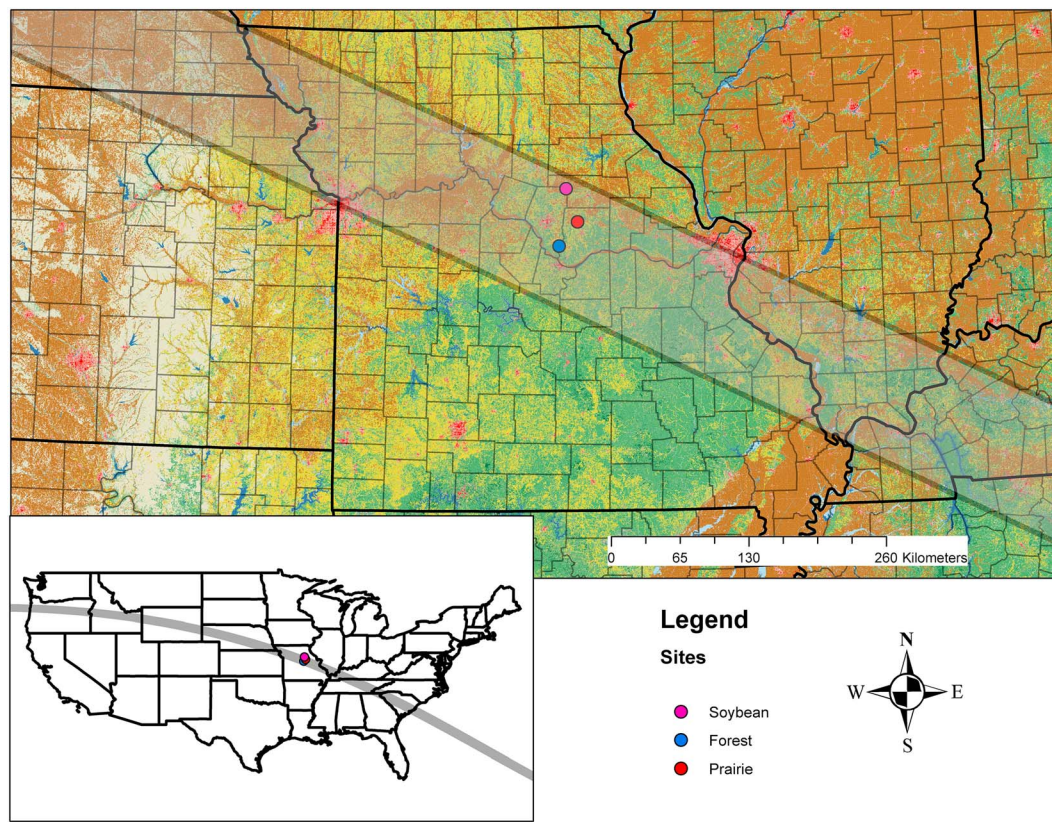


Figure 1. Locations of the three eddy covariance flux tower sites in mid-Missouri relative to the path of totality that is represented by the gray-shaded band. In the main panel, land cover (National Land Cover Database, 2011) is represented by different colors: Brown = cultivated crops, yellow = pasture/hay, light green = deciduous forest, red/pink = urban. The inset map of the conterminous United States also shows the study sites and the path of totality.

2.1.2. Prairie

The Tucker Prairie site is located at the Clair L. Kucera Research station, approximately 30 km east of Columbia MO (latitude 38.9491, longitude -92.9951). The 60-ha prairie was owned by the William C. Tucker family for 125 years and then purchased by the University of Missouri in 1957. The National Natural Landmark (designated in 1978) and State Natural Area (designated in 1998) is owned, managed, and maintained by the University of Missouri, with support from the Missouri Department of Conservation. The planosol soils have never been tilled, and the site is representative of poorly drained prairies that historically covered much of northern Missouri in the Midwest peninsular region (Dahlman & Kucera, 1965; Drew, 1947; Kucera et al., 1965). Although there are more than 200 plant species present, the main species are big bluestem (*Andropogon gerardi*) and little bluestem (*A. scoparius*; Dahlman & Kucera, 1965; Drew, 1947).

An EC system was deployed at Tucker Prairie in August of 2017 prior to the total solar eclipse. During the eclipse, the tower was equipped with only an EC system, an air temperature/humidity probe (model HMP-155A; Vaisala Inc., Boulder, CO), an upward facing pyrgeometer (model CGR3; Kipp and Zonen USA, Inc., Bohemia, NY), and an upward facing pyranometer (model CMP3; Kipp and Zonen USA, Inc.). The EC system consisted of an open-path infrared gas analyzer (model LI-7500A; Li-Cor Inc., Lincoln, NE) and a sonic-anemometer-thermometer (model WindmasterPro; Gill Instruments Ltd., Lymington, UK). All data were recorded using a data logger (model CR3000; Campbell Scientific Inc., Logan, UT).

2.1.3. Croplands

The croplands site (latitude 39.2299, longitude -92.1168) is part of the Central Mississippi River Basin Long-term Agro-Ecosystem Research network site (Sadler et al., 2015), approximately 35 km northeast of Columbia, MO. The field is under aspirational management that includes an annual winter cover crop and zero tillage (Yost et al., 2017). Prior to seeding the main crop, the cover crop is killed with herbicide and the residue left on the surface. The main crop in 2017 was soybean (*Glycine max*), and hereafter, we

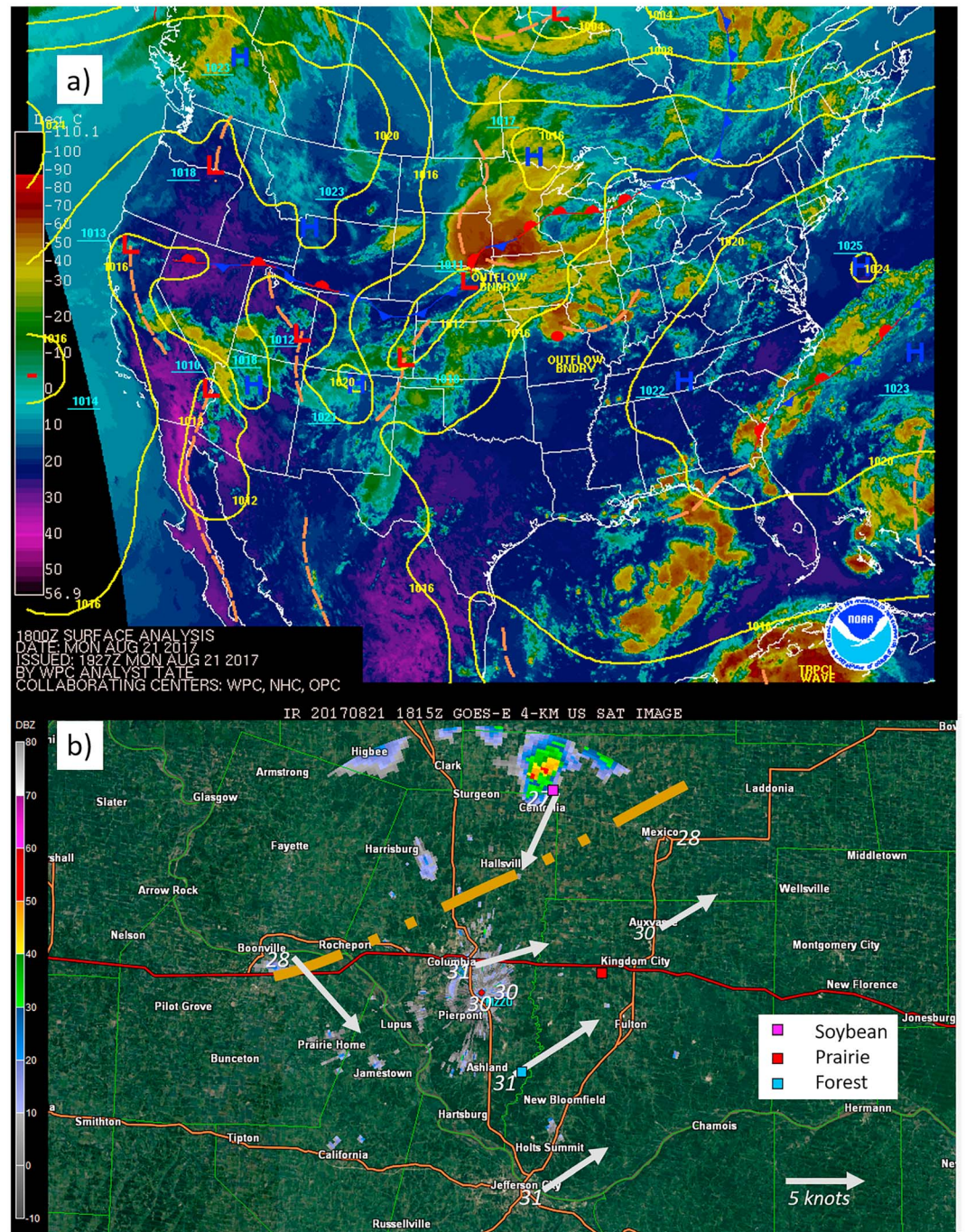


Figure 2. Meteorological analyses valid at 1200 CST 21 August 2017 of (a) the cloud cover over the continental United States, with standard surface frontal symbols, and isobars (yellow, solid; every 4 hPa), and (b) regional radar reflectivity from the MZZU radar, with 2-m surface temperatures (white text; °C), and wind vectors (white arrows; knots) at the Missouri MesoNet sites. Red dot in Figure 2a defines the region in Figure 2b. Figure 2a is modified from a plot derived from the National Centers for Environmental Prediction.

therefore refer to this field as the soybean site. The flux tower was established in 2015, and the EC system is an integrated sonic anemometer/open-path infrared gas analyzer design (model IRGASON; Campbell Scientific Inc.). A full complement of ancillary meteorological measurements including all incoming and outgoing broadband radiation components (solar, longwave, photosynthetically active), air temperature/humidity, and subsurface climate observations are also made.

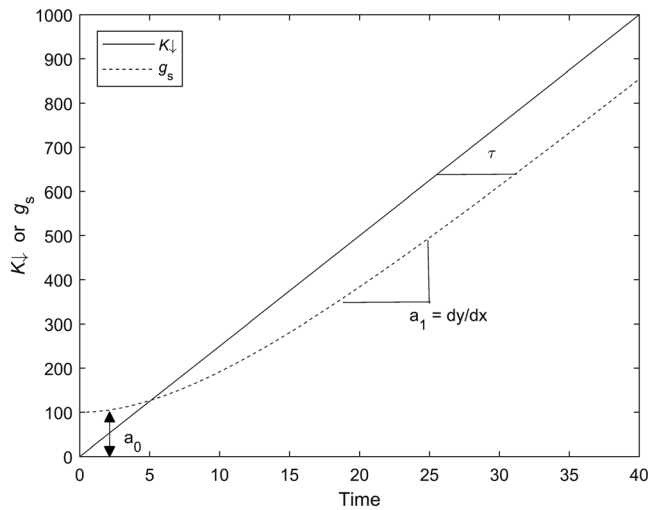


Figure 3. Example representation of the first order model used to represent the dynamic response of surface conductance (g_s) to illumination by incoming solar radiation (K_{\downarrow}), showing the physical interpretation of parameters in the model (equation (8)). The y axis units are dimensionless.

2.2. Observation Conditions

The eclipse across Missouri occurred in the maritime tropical air mass west of weak high pressure over the Deep South and south of weak low pressure over Nebraska, with an associated quasi-stationary frontal boundary stretching from the High Plains to the upper Midwest (Figure 2a). This ensured broad southwesterly flow in the atmosphere undisturbed by deep moist convection. Indeed, the satellite portion of Figure 2a highlights significant convection along and north of the frontal boundary over eastern South Dakota and southwest Minnesota, but also a secondary area of convection over north-central Missouri.

Outflow from that secondary area of convection over Missouri acted to mask the effects of the eclipse over the northern portion of the study area. Figure 2b is a plot of regional radar data valid at 1154 CST 21 August 2017, with regional surface weather observations from the standard observing network, the Missouri MesoNet, and several special observing sites, all from the 1150–1200 CST time range. A homogenous air mass existed at and south of the radar, with similar temperatures and wind directions. Two northern locations, Boonville and Centralia, MO, experienced the passage of the convective outflow boundary at ~1145 CST. Although temperatures were cool at the third northern location, Auxvasse, MO, the

winds there were calm at the time of the analysis, and were southwesterly both prior to and after this analysis time.

The soybean field was the only flux tower site where the eclipse forcing was contaminated by mesoscale meteorology (Figure 2). This complicated the full cross-site comparison. Therefore, in some cases analyses were not performed at all sites when not appropriate.

2.3. Data Analysis

2.3.1. Wavelet-Based Fluxes

When advection and horizontal turbulent fluxes are negligible, the net ecosystem flux (F_N) is equal to the sum of the eddy flux (F_E) and the storage flux (F_S ; Gu et al., 2012; Leuning, 2004, 2007): $F_N = F_E + F_S$ (see supporting information for further details). The F_E is obtained from the eddy covariance (EC) measurements, while F_S is best obtained from profile observations below the EC system. The F_S term is generally negligible in systems with short-statured vegetation (e.g., prairies and croplands). In contrast, F_S is often nontrivial in forests with tall, complex canopies when turbulence is weak, and becomes less important during daytime conditions with well-developed turbulence. Typically, fluxes are calculated for 30- or 60-min averaging periods. The abrupt changes in solar forcing during the eclipse give rise to nonstationary conditions and atmospheric dynamics that were expected to vary on time scales shorter than the typical 30- or 60-min averaging periods. We were interested in probing these dynamics and therefore adopted a wavelet-based approach to calculate F_E at 2-min resolution and neglected F_S . Further details regarding the implications of neglecting F_S can be found in the supporting information.

Wavelet-based approaches are particularly suited for probing nonstationary data (Grinsted et al., 2004; Torrence & Compo, 1998) and were thus used to study the flux responses to this total eclipse. Similar wavelet-based approaches have been previously used to examine atmospheric turbulence and compute turbulent fluxes (Desjardins et al., 2018; Mauder et al., 2007; Xu et al., 2017).

A brief description of relevant methods is provided here; however, for a more thorough treatment of wavelet theory and applications, the reader is referred to the literature (Desjardins et al., 2018; Grinsted et al., 2004; Mauder et al., 2007; Torrence & Compo, 1998; Xu et al., 2017). For a signal, x , the wavelet transform gives a set of coefficients, $W_n^X(s)$, for all times (n) and for a set of predefined scales, s (which represents frequency-space). Upon obtaining $W_n^X(s)$, the wavelet power spectrum, $E_X(s)$, is obtained as $|W_n^X(s)|^2$. The wavelet power spectrum can be averaged across time according to

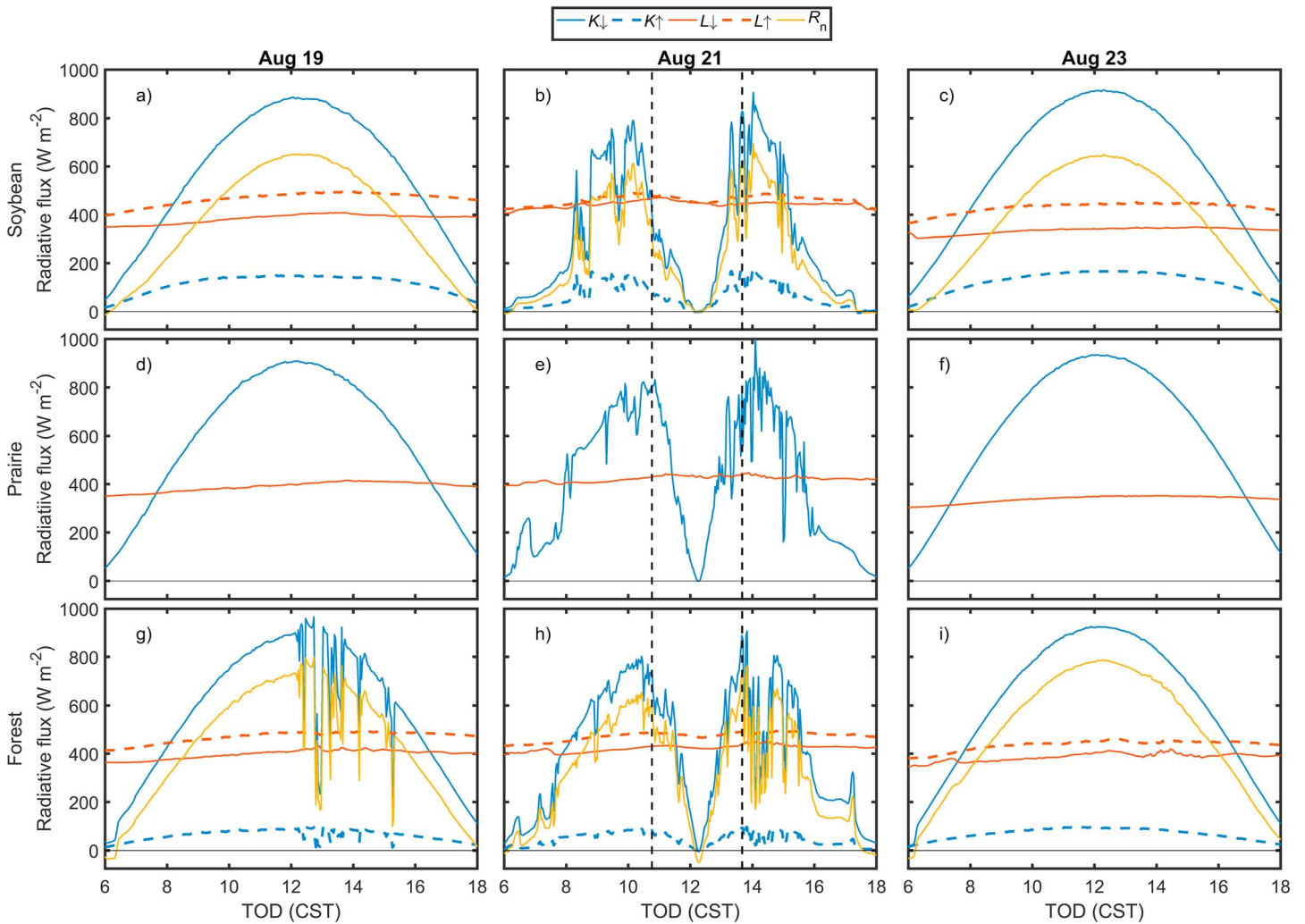


Figure 4. Diurnal cycles (TOD = time of day; CST = Central Standard Time) of radiation fluxes (2-min means) on the (middle column) day of the eclipse (21 August 2017) and clear-sky reference days (left column) before (19 August 2017) and (right column) after (23 August 2017) the eclipse at the (a–c) soybean, (d–f) prairie, and (g–i) forest sites. K_{\downarrow} = incoming solar radiation (solid blue line), K_{\uparrow} = outgoing solar radiation (dashed blue line), L_{\downarrow} = incoming longwave radiation (solid red line), L_{\uparrow} = outgoing longwave radiation (dashed red line), R_n = net radiation (yellow line). The only radiation fluxes measured at the prairie sites were the incoming components (K_{\downarrow} and L_{\downarrow}). The vertical dashed lines in the middle column panels represent the timing of eclipse first and fourth contacts.

$$E_X(s) = \frac{\delta t}{C_{\delta} N} \sum_{n=0}^{N-1} |W_n^X(s)|^2 \quad (1)$$

where δt is the sampling interval, C_{δ} is the wavelet reconstruction factor that was set to 0.776 (Torrence & Compo, 1998), and N is the number of observations (in time). When averaged across all times as in equation (1), one obtains the global wavelet spectrum, which is analogous to the Fourier spectrum. The total variance, σ_X^2 , of the $E_X(s)$ spectrum is obtained by integrating across scales:

$$\sigma_X^2 = \delta j \sum_{j=0}^{J-1} \frac{E_X(j)}{s(j)} \quad (2)$$

where δj is the nondimensional and is the number of scales per octave (set to 1/12 here; Grinsted et al., 2004), and j indexes scales.

We can also obtain the cross-wavelet transform of two signals, x and y , from their respective wavelet coefficients according to $W_n^X(s)W_n^Y(s)^*$, where $*$ represents the complex conjugation of the wavelet coefficients for the y signal. The average cross-spectrum is obtained from

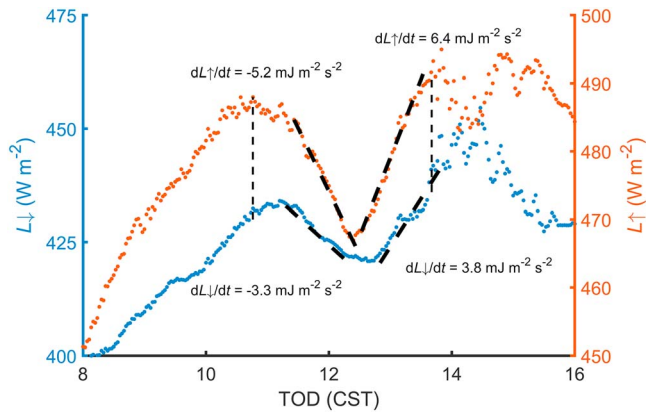


Figure 5. Rates of change of incoming (L_{\downarrow} ; blue dots) and outgoing (L_{\uparrow} ; red dots) longwave radiation at the forest site during the eclipse on 21 August 2017. The vertical dashed lines represent the timing of eclipse first and fourth contacts (TOD = time of day; CST = Central Standard Time).

$$E_{XY}(s) = \frac{\delta t}{C_{\delta} N} \sum_{n=0}^{N-1} W_n^X(s) W_n^Y(s)^* \quad (3)$$

The cospectrum is obtained from the real component of $E_{XY}(s)$, and integration of the cospectrum yields the covariance of signals x and y (cov_{xy}):

$$\text{cov}_{XY} = \delta j \sum_{j=0}^{J-1} \frac{\Re[E_{XY}(j)]}{s(j)} \quad (4)$$

Note that the averaging across time in equations (1) and (3) need not be applied to the complete signal and can instead be implemented at shorter levels of temporal aggregation. Similarly, the integration across scale as in equations (2) and (4) can be carried out across a subset of scales, which is particularly useful where edge effects associated with the transform are important, and it is desirable to integrate only those scales that are within the cone of influence (Desjardins et al., 2018; Mauder et al., 2007). Example wavelet cross spectra that were averaged (equation (3)) and inte-

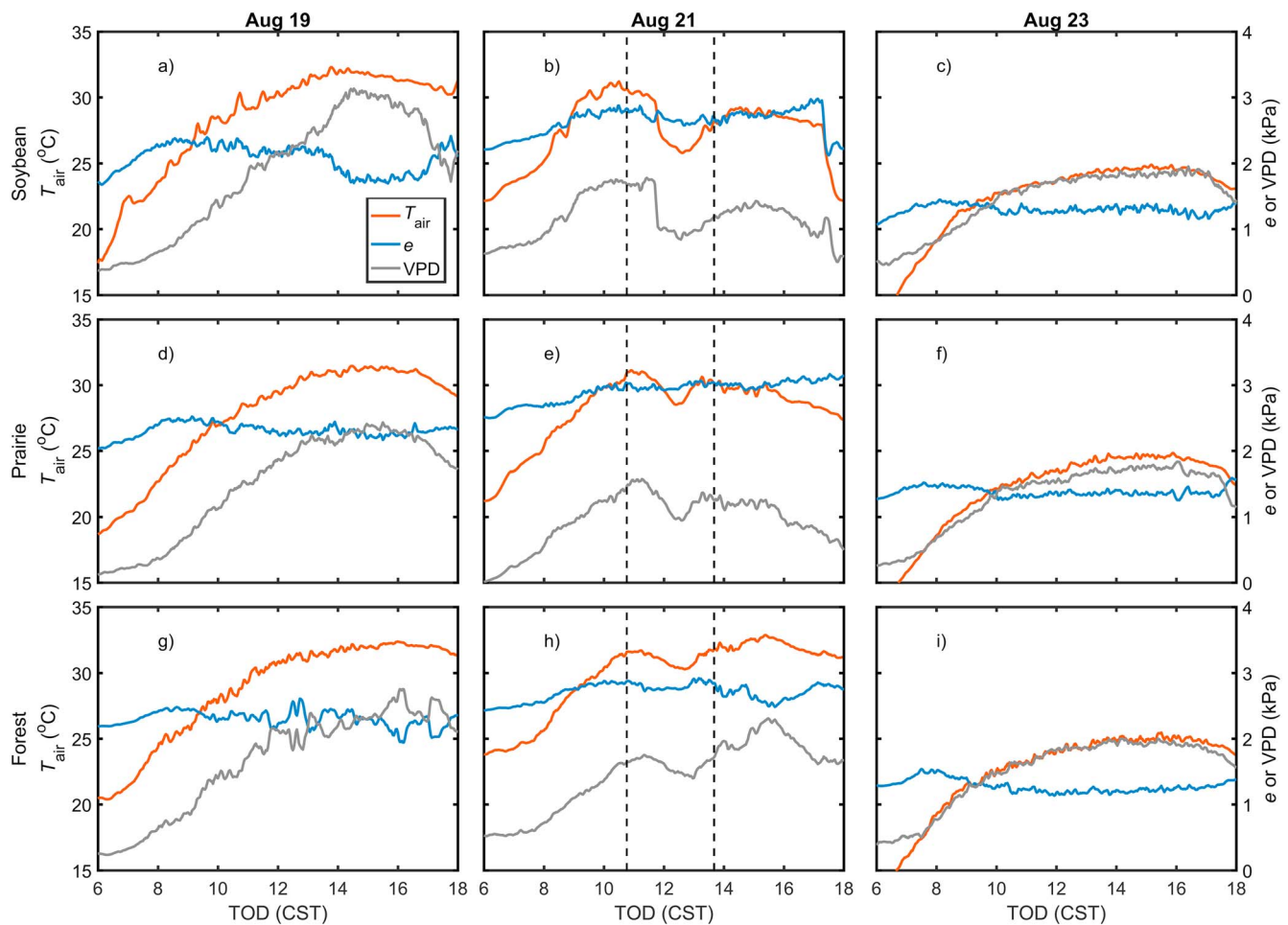


Figure 6. Diurnal cycles (TOD = time of day, CST = Central Standard Time) of 2-min mean air temperature (T_a ; red lines), vapor pressure (e ; blue lines), and atmospheric vapor pressure deficit (VPD; gray lines) on (middle column) the day of the eclipse (21 August 2017) and clear-sky reference days (left column) before (19 August 2017) and (right column) after (23 August 2017) the eclipse at the (a–c) soybean, (d–f) prairie, and (g–i) forest sites. The vertical dashed lines in the middle column panels represent the timing of eclipse first and fourth contacts.

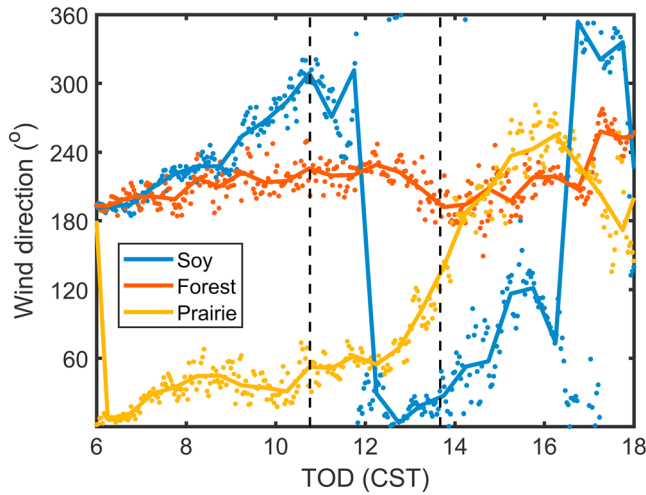


Figure 7. Mean wind directions at the soybean, prairie, and forest sites on the day of the eclipse (21 August 2017). The circles and lines represent 2- and 30-min means, respectively. The vertical dashed lines represent the timing of eclipse first and fourth contacts (TOD = time of day, CST = Central Standard Time).

grated (equation (4)) to obtain covariances for flux calculations are shown for the day of the eclipse in Figure S3.

The data processing used here consisted of the following steps. High-frequency data were first screened for spikes, and the instantaneous wind velocities rotated into the planar fit coordinate system (Wilczak et al., 2001). Wavelet transforms on the vertical wind velocity (w) and scalar time series were then implemented using the Morlet mother wavelet, which has been used in previous studies of atmospheric turbulence (Desjardins et al., 2018; Mauder et al., 2007; Xu et al., 2017), and for which wavelet scale maps closely to an equivalent Fourier period ($\lambda = 1.03$ s). The code described in Grinsted et al. (2004) was used to perform all wavelet analyses. We computed 2-min variances (equation (2)) and covariances (equation (4)), integrating across scales up to 15 min for the prairie and soybean sites, and up to 30 min at the forest site because low-frequency contributions to the flux were significant over the tall, rough forest vegetation and higher measurement height, z . Once the covariances were computed according to equation (4), the eddy fluxes of LE and H heat were obtained from a simultaneous solution to the equations of Schotanus et al. (1983) and Webb et al. (1980) as described in Baker and Griffis (2005) which ultimately gives (in standard Reynolds notation)

$$LE = \frac{\lambda \overline{\rho w' q'}}{1 - \overline{q'}} \quad \text{and} \quad (5)$$

$$H = \overline{\rho c_p w' T'} \quad (6)$$

where w is the vertical wind velocity (m/s), q is the specific humidity (g/g), $\overline{\rho}$ is the mean air density (g/m^3), λ is the latent heat of vaporization (J/g), c_p is the specific heat capacity of air at constant pressure ($\text{J g}^{-1} \text{K}^{-1}$), T is the temperature (K), overbars represent the time averaging, and primes the perturbation from the time average. Atmospheric stability was assessed using the dimensionless stability parameter, $\zeta = (z - d)/L$, where z is the measurement height (m), d is the height of zero plane displacement (m) that was assumed equal to 2/3 the canopy height, and L is the Obukhov length (m). The atmosphere is unstable when $\zeta < 0$ and is stable for $\zeta > 0$.

2.3.2. Surface Conductance and Atmospheric Coupling

The surface conductance (g_s) was obtained by inverting the Penman-Monteith equation and substituting the turbulent energy fluxes for available energy (Zhang et al., 2006):

$$\frac{1}{g_s} = \frac{\rho c_p D}{\gamma \cdot LE} + \frac{(Bs/\gamma) - 1}{g_a} \quad (7)$$

where ρ is the air density (kg/m^3), c_p is the constant pressure specific heat capacity of air ($\text{J} \cdot \text{kg}^{-1} \cdot \text{K}^{-1}$), D is the vapor pressure deficit of the air (kPa), B is the Bowen ratio ($=H/LE$), s is the rate of change of saturated vapor pressure with temperature (kPa/K), γ is the psychrometric constant (kPa/K), and g_a is the aerodynamic conductance, which was parameterized according to $g_a^{-1} = u_*^{-2} + 6.2u_*^{-0.67}$ (Monteith & Unsworth, 1990), where u_* is the friction velocity (m/s). Note that as formulated, all conductances carry units of m/s, but were subsequently converted to units of $\text{mmol} \cdot \text{m}^{-2} \cdot \text{s}^{-1}$. Turbulent energy fluxes ($=H + LE$; from EC measurements) were substituted for available energy (Pingintha et al., 2010; Zhang et al., 2006) because the measurement footprint of the former is larger and a better integrator over the ecosystem versus available energy determined from observations of net radiation and ground heat flux. The g_s obtained here is largely representative of canopy stomatal conductance; however, it contains nonleaf contributions to evapotranspiration because the measured LE is the sum of evaporation from the soil and surface wetness (if present) and transpiration expressed per unit ground area. We were concerned with periods where there was no surface wetness and canopies were fully closed. Therefore, LE and g_s were dominated by transpiration and canopy stomatal contributions, respectively.

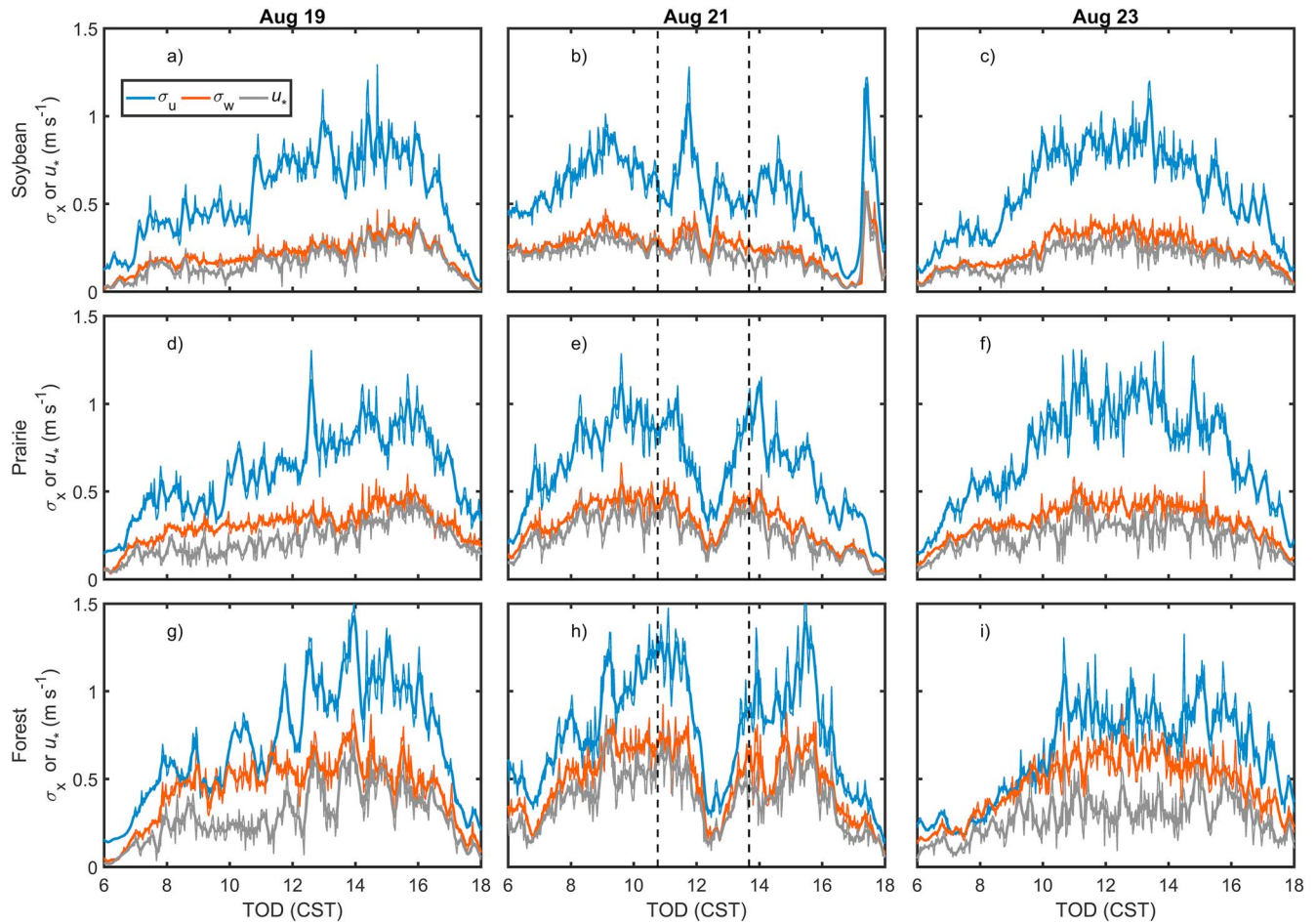


Figure 8. Diurnal cycles (TOD = time of day, CST = Central Standard Time) of wavelet-based standard deviations of the stream-wise horizontal wind (σ_u ; blue lines) and vertical wind velocities (σ_w ; red lines), and the friction velocity (u^* ; gray lines) on (middle column) the day of the eclipse (21 August 2017) and clear-sky reference days (left column) before (19 August 2017) and (right column) after (23 August 2017) the eclipse at the (a–c) soybean, (d–f) prairie, and (g–i) forest sites. Thin lines represent data at 2-min resolution, and the thick lines, 10-min running means. The vertical dashed lines in the middle column panels represent the timing of eclipse first and fourth contacts.

2.3.3. Time Constant of the Surface Conductance Light Response

The eclipse offered the unique opportunity to estimate the time constant of the g_s light response. The temporal g_s dynamics were modeled using data from between third and fourth contacts when K_d increased linearly and was free from contamination by clouds. Assuming a first-order system, the g_s response to a linear incoming solar radiation (K_d) ramp input was modeled according to

$$g_s(t) = a_0 + a_1 t - a_1 \tau (1 - e^{-t/\tau}) \quad (8)$$

where τ is the g_s time constant (min). Equation (8) is similar in form to the classic solution to the problem of an output to a ramp input for a first-order system (Brock & Richardson, 2001); however, an offset term (a_0) has been added here to account for a nonzero minimum g_s at totality. A theoretical representation of the model (equation (8)) and its relationship to K_d is provided in Figure 3. The physical interpretation of τ is the time required for g_s to achieve a 63.2% response to a step change in light levels. In the case of the response to a linear ramp increase in light, τ is the lag time between K_d and g_s at steady state. Note that it was only possible to compute τ for the prairie site because the mesoscale convective activity contaminated the eclipse forcing at the soybean field, and at the forest site the canopy was decoupled from atmospheric turbulence around totality because of strong stabilization of the surface layer.

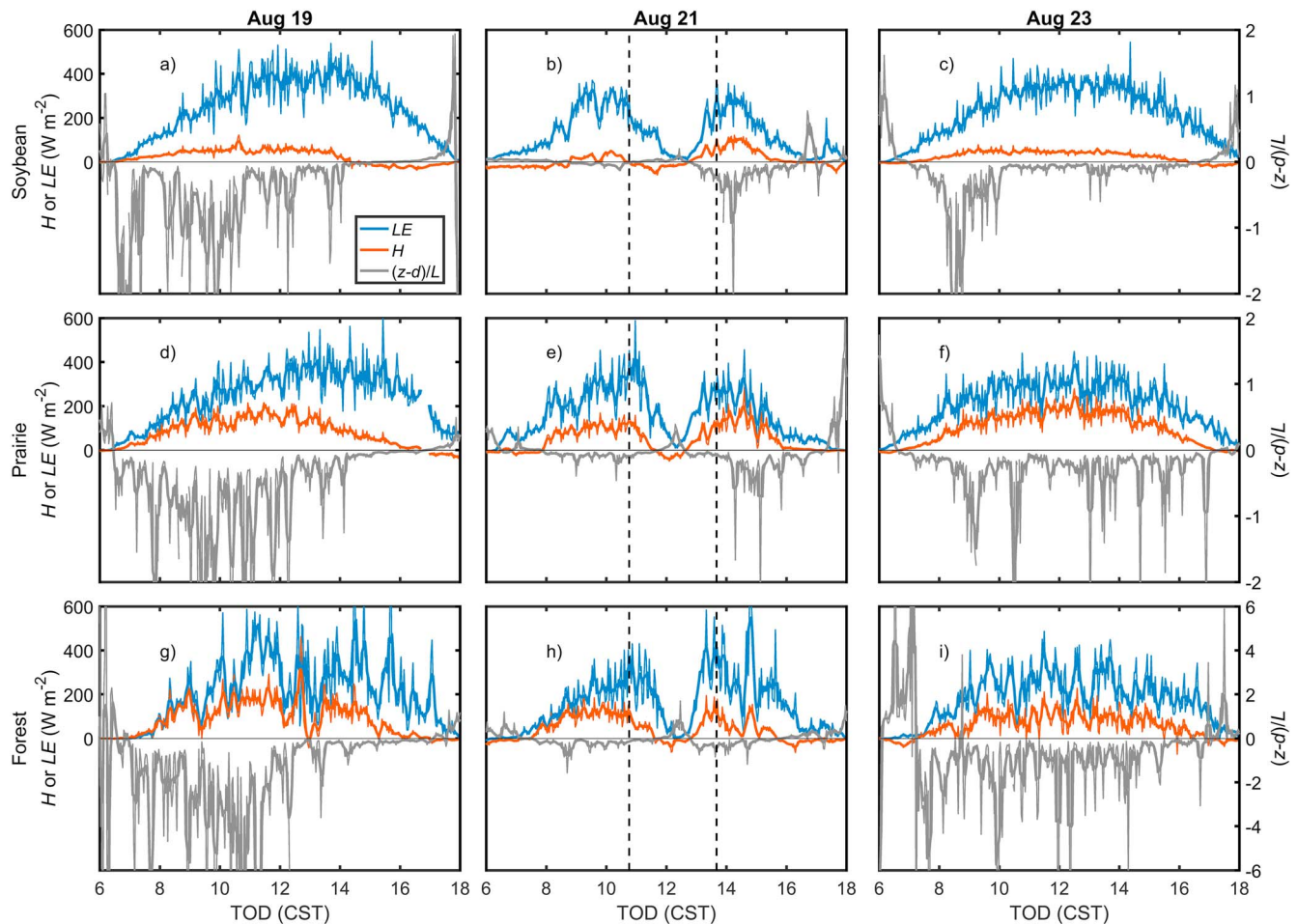


Figure 9. Diurnal cycles (TOD = time of day, CST = Central Standard Time) of wavelet-based eddy fluxes of latent (LE ; blue lines) and sensible (H ; red lines) heat, and the dimensionless stability parameter, $(z - d)/L$ (gray lines), on (middle column) the day of the eclipse (21 August 2017) and clear-sky reference days (left column) before (19 August 2017) and (right column) after (23 August 2017) the eclipse at the (a–c) soybean, (d–f) prairie, and (g–i) forest sites. Note that the y axis scale for dimensionless stability in the bottom row is different from the top two. Thin lines represent data at 2-min resolution, and the thick lines, 10-min running means. The vertical dashed lines in the middle column panels represent the timing of eclipse first and fourth contacts. z = measurement height, d = height of zero plane displacement (estimated as $2/3$ canopy height), L = Obukhov length.

3. Results

3.1. Meteorology and Radiation

Strong eclipse signals in terms of radiation fluxes were observed at the eddy flux towers (Figures 4b, 4e, and 4h). There was, however, variable cloudiness at the forest and prairie sites (Figures 4b, 4e, and 4h), and observations at the soybean field were contaminated by convective activity according to surface weather analysis and radar observations (Figure 2). Radiation observations on clear-sky days flanking the eclipse are also provided for reference (Figures 4a, 4c, 4d, 4f, 4g, and 4i). During the eclipse at the soybean field, thick cloud cover decreased K_{\downarrow} approximately 1 hr before first contact, “smearing” the signal (Figure 4b) due to higher relative contributions from diffuse solar radiation. In contrast, the forest and prairie sites experienced scattered clouds pre-eclipse and post-eclipse, giving rise to relatively sharp eclipse signals between first and fourth contacts albeit with some cloudiness in the earliest and latest stages of the eclipse, whereby K_{\downarrow} decreased from ~ 800 to 0 W/m^2 at maximum obscuration, followed by an increase to $\sim 800 \text{ W/m}^2$. At the forest site, the longwave radiative cooling and heating rates of the surface (atmosphere) attributable to the eclipse were $-5.2 \text{ mJ}\cdot\text{m}^{-2}\cdot\text{s}^{-2}$ ($-3.3 \text{ mJ}\cdot\text{m}^{-2}\cdot\text{s}^{-2}$) and $6.4 \text{ mJ}\cdot\text{m}^{-2}\cdot\text{s}^{-2}$ ($3.8 \text{ mJ}\cdot\text{m}^{-2}\cdot\text{s}^{-2}$), respectively, with a noticeable phase lag for the atmospheric signal (Figure 5). The longwave atmospheric cooling rate was the same at

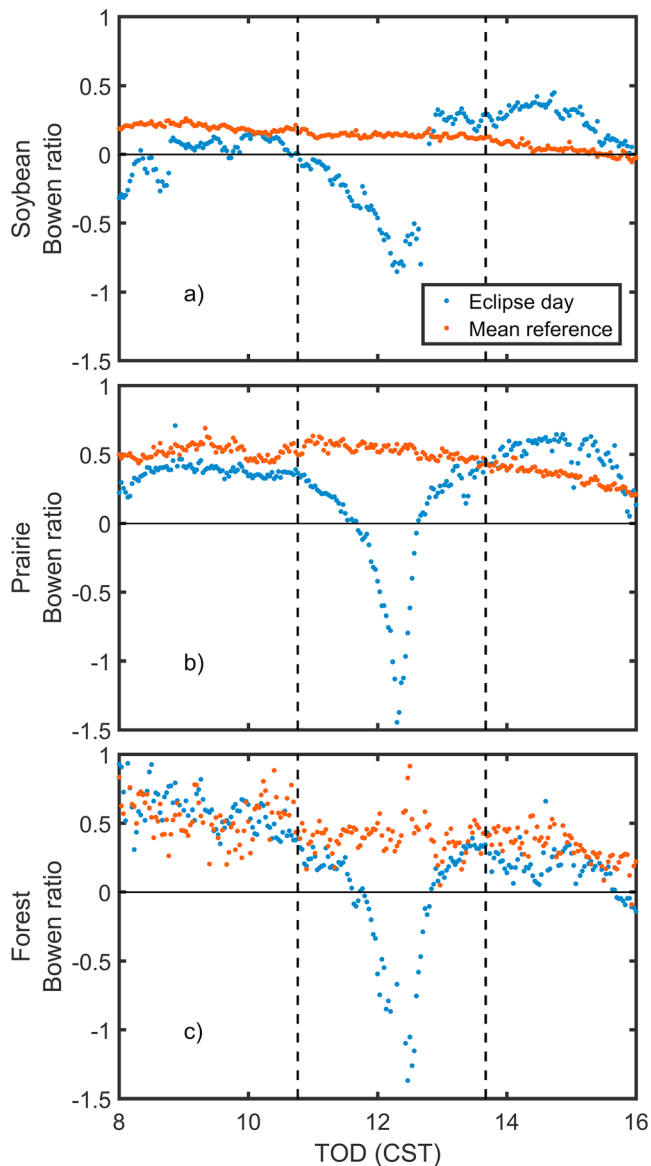


Figure 10. Diurnal cycle (TOD = time of day, CST = Central Standard Time) of the Bowen ratio ($=H/LE$) for the (a) soybean, (b) prairie, and (c) forest sites. The mean reference symbols are the mean of observations on clear-sky reference days (19 and 23 August 2017) flanking the eclipse day (21 August 2017).

the prairie site ($-3.3 \text{ mJ}\cdot\text{m}^{-2}\cdot\text{s}^{-2}$; data not shown), but surface radiative heating/cooling rates could not be estimated because outgoing longwave measurements were not available.

From first contact to totality, air temperatures decreased by 5.0°C , 2.5°C , and 1.5°C at the soybean, prairie, and forest sites, respectively (Figures 6b, 6e, and 6h). The comparatively large-temperature response at the soybean site was primarily due to cold outflow from convective systems to the north (Figure 2) as evidenced by the precipitous temperature drop (Figure 6b) between first and second contacts (Table 1) that coincided with a large change in wind direction (Figure 7). Air temperatures at the soybean and prairie sites did not recover to preeclipse values because of cloudiness in the afternoon. Atmospheric vapor pressures showed little variation throughout the eclipse, but there was a comparatively large drop in vapor pressure deficit due to changes in T_{air} (Figures 6b, 6e, and 6h).

3.2. Micrometeorology

In general, the intensity of turbulence was greater over the aerodynamically rough forest versus the smoother soybeans and prairie (Figure 8). The eclipse had a marked effect on atmospheric turbulence (Figures 8b, 8e, and 8h) and energy fluxes (Figures 9b, 9e, and 9h). At the forest (aerodynamically rough) and the prairie (aerodynamically smooth), the standard deviations of the horizontal and vertical wind velocities and friction velocities (Figures 8e and 8h) decreased by $\sim 75\%$ and $\sim 60\%$, respectively, during the eclipse. At the soybean field, where the eclipse effect was contaminated by mesoscale meteorology, there was a local σ_u maximum between first and second contacts that coincided with the passage of a gust front (Figure 8b), followed by a local minimum that was consistent with observations at the prairie and forest sites (Figures 8e and 8h).

On clear-sky days without the eclipse, LE and H daytime peaks at all sites were on the order of $300\text{--}400$ and $50\text{--}200 \text{ W/m}^2$ (Figures 9a, 9c, 9d, 9f, 9g, and 9i), with the range in maxima related to differences in peak T_{air} and VPD (Figures 6a, 6c, 6d, 6f, 6g, and 6i), and ecosystem physiology. The partitioning of available energy into H and LE differed markedly across ecosystems, with lower Bowen ratios ($B = H/LE$) in soybeans ($B = 0.09 \pm 0.005$; mean \pm standard error) versus the prairie ($B = 0.40 \pm 0.007$) and forest ($B = 0.43 \pm 0.021$; Figure 10), which had important implications on atmospheric stability (Figure 9). The atmosphere was generally unstable during daytime noneclipse conditions at all three sites; however, instability (based on dimensionless stability parameter) was greatest over the forest ($\zeta = -1.06 \pm 0.088$), then the prairie

($\zeta = -0.34 \pm 0.022$) and lowest over soybeans ($\zeta = -0.24 \pm 0.018$). The eclipse induced large declines in both H and LE that were highly coherent with the solar forcing. Both LE and H lagged K_{\downarrow} by <5 min at all sites. The direction of the sensible heat flux changed during the eclipse and was directed from the atmosphere to the surface for $\sim 35\%$ of the time between first and fourth contacts at sites not affected by mesoscale convective activity (forest and prairie). In contrast, LE approached 0 W/m^2 , but did not change in direction (minimum LE was $\sim 10 \text{ W/m}^2$ at prairie and soybean sites and $\sim 0 \text{ W/m}^2$ at the forest). At totality, Bowen ratio local minima were on the order of -0.9 to -1.5 (Figure 10) accompanied by a peak in the atmospheric stability parameter (Figure 9). The eclipse-induced stabilization of the atmosphere was stronger at the forest ($\zeta = 0.45 \pm 0.097$) than at the prairie ($\zeta = 0.21 \pm 0.037$), which may have been caused by the former being closer to the center of the path of totality, where there was greater suppression of turbulence and vertical atmospheric motions (Figures 8e, 8h, 9e, and 9h).

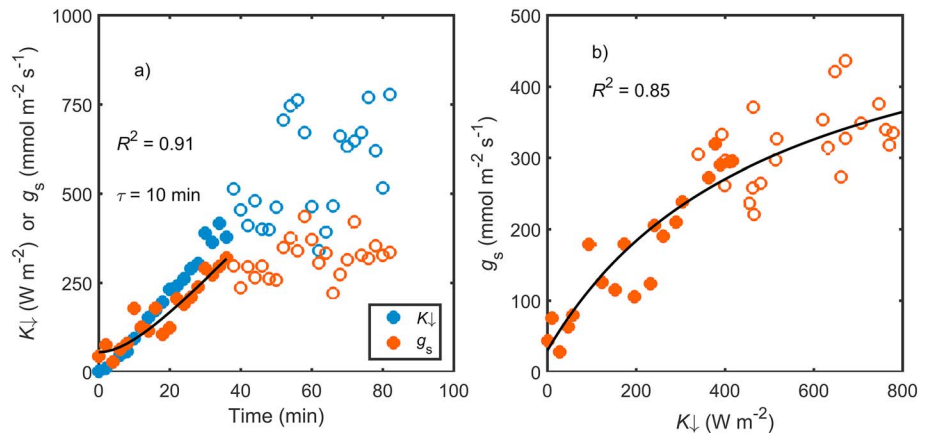


Figure 11. The (a) time series of 2-min mean incoming solar radiation (K_{\downarrow}) and surface conductance (g_s) and (b) the g_s light response at the prairie site. The data from between totality and fourth contact in (a) were used for determining the time constant (τ) of the g_s light response (only the filled symbols were used in modeling τ , and the black line is the model fit). At steady state, τ is equal to the time lag between K_{\downarrow} and g_s . A rectangular hyperbola ($g_s = \alpha\beta/[\alpha K_{\downarrow} + \beta]$) was used to model the g_s light response in (b), and was fit to all observations (filled symbols correspond to those used for determining the time constant).

The temporal dynamics of the g_s light response at the prairie were probed by determining the time constant when K_{\downarrow} increased linearly after totality. The linear ramp increase of K_{\downarrow} between third and fourth contacts lasted for only ~ 40 min because of increasing cloudiness toward the end of the eclipse. During these ~ 40 min, the g_s time constant, τ , was found to be 10 min (Figure 11a). A rectangular hyperbola ($g_s = \alpha\beta/[\alpha K_{\downarrow} + \beta]$) model (fit using all data between third and fourth contacts) revealed the classic response of g_s saturation at high light (Figure 11b).

4. Discussion

Mid-Missouri was ideally situated for an investigation of eclipse micrometeorology because the timing of totality was coincident with solar noon (Figure S1). Unfortunately, there was mesoscale convective activity in the northern part of our study domain that had a significant effect on observations at the soybean field. Although the forest and prairie sites experienced variable cloudiness, strong eclipse signals were observed (Figures 4 and 6–9) and there was a break in clouds around (± 15 min) totality (Figure 4). At sites that were unaffected by convective activity (forest and prairie), there was a particularly strong eclipse effect that elicited rapid declines and increases in σ_w , σ_w , LE , and H . In general, the dynamics of air temperature, turbulence, radiation, and energy fluxes and stability displayed the expected responses to the eclipse solar forcing (Antonia et al., 1979; Eaton et al., 1997; Foken et al., 2001; Mauder et al., 2007; Stewart & Rouse, 1974; Turner et al., 2018). There were large changes in the surface energy balance between first and fourth contacts, with LE being completely suppressed and the direction of H changing from away from to toward the surface, which resulted in a strong stabilization of the surface layer (Figures 9e and 9h). The stable surface layer during the eclipse was flanked by very unstable conditions before and after, which is typical for a day in August. In Oklahoma, where the maximum obscuration was only 89%, the boundary layer dynamics showed a similar pattern: a convective boundary layer of ~ 1.3 -km depth collapsed to a stable boundary layer (~ 200 – 300 -m depth) during the eclipse, and became convective again (~ 1.3 -km depth) afterward (Turner et al., 2018). Although we observed large variations in K_{\downarrow} , R_n , LE , and H , the concomitant decreases in T_{air} were relatively muted at ~ 1.5 – 2.5 °C (Figures 6e and 6h). These T_{air} reductions were, however, broadly consistent with the lower end of estimates for nine U.S. Climate Reference Network stations (2 – 5 °C) that were in the path of totality in locations spanning from Oregon to South Carolina (Burt, 2018; Lee et al., 2018). It is noteworthy that there were anecdotal reports of T_{air} reductions on the order of 11 °C (where cold air drainage from mountains was important). The muted T_{air} reductions in Missouri were likely a combination of the lack of orographic effects due to relatively flat topography and humid conditions that confer higher thermal inertia.

A deeper probing of ecosystem physiological responses was accomplished by determining the τ of the g_s light response. This analysis was restricted to the prairie site because of the contamination of the eclipse signal by mesoscale meteorology at the soybean field, and the forest canopy being decoupled from surface layer turbulence due to strong stabilization during totality. The τ for the g_s light response was 10 min for the prairie (Figure 11a), and the classic g_s light response curve had a rectangular hyperbolic form (Figure 11b). The canopy-scale estimate of τ is in reasonable agreement with leaf-level estimates for prairie plant species (Knapp, 1993; Vico et al., 2011). It is comforting that inverting the simple, single-layer (i.e., big-leaf) Penman-Monteith model (Raupach & Finnigan, 1988) yields physiologically realistic canopy-scale g_s behavior, even when pushing the envelope and forcing with 2-min average data (although the wavelet energy fluxes do contain low-frequency flux contributions due to the nature of the calculation).

5. Conclusions

During the total solar eclipse of 21 August 2017, Mid-Missouri experienced ~ 2 min 40 s of totality. Here we report on the micrometeorology over three ecosystems that contrasted in their structure and physiology. At one of our sites (soybean), the eclipse effect was contaminated by mesoscale convective activity; however, at the other two (forest and prairie), there was only variable cloudiness that dissipated around totality. We documented large solar eclipse forcings that significantly altered turbulence, surface energy balances, and atmospheric stability. Although there were large variations in LE and H , which approached 0 W/m^2 and changed direction, respectively, the temperature reduction (~ 1.5 – $2.5 \text{ }^\circ\text{C}$) was rather muted. The rare radiation environment afforded by the eclipse allowed us to estimate physiologically realistic canopy-scale time constant of the g_s light response for a prairie ($\tau = 10$ min) that is consistent with leaf-level measurements.

In closing, we wish to highlight that here we report only on the micrometeorological component of the Mid-Missouri Eclipse Meteorological Experiment. Perhaps the most important aspect of this work was that the eclipse captured public attention, which generated much interest in science and engaging with researchers. The importance of science education cannot be understated, and rare events that garner intense interest from the public such as an eclipse can serve as the starting point of a larger conversation. It is therefore crucial to leverage these opportunities that can support improving the general science literacy of the public.

Acknowledgments

This work was partially supported by funding from NASA (grant NNX17AH79G) through the Interdisciplinary Science For Eclipse 2017 program. This material is based upon work supported by the U.S. Department of Energy, Office of Science, Office of Biological and Environmental Research Program, Climate and Environmental Sciences Division through Oak Ridge National Laboratory's Terrestrial Ecosystem Science-Science Focus Area (J.D.W. and L.G.). ORNL is managed by UT-Battelle, LLC, for the U.S. Department of Energy under contract DE-AC05-00OR22725. E.J.S. and J.D.W. acknowledge support by USDA-ARS Project 5070-12130-005-00D, "Long-term management of water resources in the Central Mississippi River Basin" for the soybean and prairie sites. This material is based upon work supported by the National Science Foundation under award IIA-1355406 (N.I.F., P.A.M., and A.R.L.). Any opinions, findings, and conclusions or recommendations expressed in this material are those of the author(s) and do not necessarily reflect the views of the National Science Foundation. Tucker Prairie is a preserve of the University of Missouri and managed by the Division of Biological Sciences. The data analyzed in this research will be made available upon publication through Oak Ridge National Lab's Terrestrial Ecosystem Science Focus Area data portal.

References

- Anderson, J. (1999). Meteorological changes during a solar eclipse. *Weather*, *54*(7), 207–215. <https://doi.org/10.1002/j.1477-8696.1999.tb06465.x>
- Antonia, R. A., Chambers, A. J., Phong-Anant, D., Rajogopalan, S., & Sreenivasan, K. R. (1979). Responses of atmospheric surface layer turbulence to a partial solar eclipse. *Journal of Geophysical Research*, *84*(C4), 1689–1692. <https://doi.org/10.1029/JC084iC04p01689>
- Aplin, K. L., Scott, C. J., & Gray, S. L. (2016). Atmospheric changes from solar eclipses. *Philosophical Transactions of the Royal Society A*, *374*(2077), 20150217. <https://doi.org/10.1098/rsta.2015.0217>
- Baker, J. M., & Griffis, T. J. (2005). Examining strategies to improve the carbon balance of corn/soybean agriculture using eddy covariance and mass balance techniques. *Agricultural and Forest Meteorology*, *128*(3–4), 163–177. <https://doi.org/10.1016/j.agrformet.2004.11.005>
- Brock, F. V., & Richardson, S. J. (2001). *Meteorological Measurement Systems* (1st ed.). New York: Oxford University Press Inc.
- Burt, S. (2018). Meteorological impacts of the total solar eclipse of 21 August 2017. *Weather*, *73*(3), 90–95. <https://doi.org/10.1002/wea.3210>
- Dahlman, R. C., & Kucera, C. L. (1965). Root productivity and turnover in native prairie. *Ecology*, *46*(1–2), 84–89. <https://doi.org/10.2307/1935260>
- Desjardins, R. L., Worth, D. E., Pattey, E., VanderZaag, A., Srinivasan, R., Mauder, M., et al. (2018). The challenge of reconciling bottom-up agricultural methane emissions inventories with top-down measurements. *Agricultural and Forest Meteorology*, *248*, 48–59. <https://doi.org/10.1016/j.agrformet.2017.09.003>
- Drew, W. B. (1947). Floristic composition of grazed and ungrazed prairie vegetation in north-central Missouri. *Ecology*, *28*(1), 26–41. <https://doi.org/10.2307/1932915>
- Eaton, F. D., Hines, J. R., Hatch, W. H., Cionco, R. M., Byers, J., Garvey, D., & Miller, D. R. (1997). Solar eclipse effects observed in the planetary boundary layer over a desert. *Boundary-Layer Meteorology*, *83*(2), 331–346. <https://doi.org/10.1023/A:1000219210055>
- Foken, T., Wichura, B., Klemm, O., Gerchau, J., Winterhalter, M., & Weidinger, T. (2001). Micrometeorological measurements during the total solar eclipse of August 11, 1999. *Meteorologische Zeitschrift*, *10*(3), 171–178. <https://doi.org/10.1127/0941-2948/2001/0010-0171>
- Gerasopoulos, E., Zerefos, C. S., Tsagouri, I., Founda, D., Amiridis, V., Bais, A. F., et al. (2008). The total solar eclipse of March 2006: Overview. *Atmospheric Chemistry and Physics*, *8*(17), 5205–5220. <https://doi.org/10.5194/acp-8-5205-2008>
- Grinsted, A., Moore, J. C., & Jevrejeva, S. (2004). Application of the cross wavelet transform and wavelet coherence to geophysical timeseries. *Nonlinear Processes in Geophysics*, *11*(5–6), 561–566. <https://doi.org/10.5194/npg-11-561-2004>
- Gu, L., Massman, W. J., Leuning, R., Pallardy, S. G., Meyers, T., Hanson, P. J., et al. (2012). The fundamental equation of eddy covariance and its application in flux measurements. *Agricultural and Forest Meteorology*, *152*(1), 135–148. <https://doi.org/10.1016/j.agrformet.2011.09.014>
- Gu, L., Pallardy, S. G., Hosman, K. P., & Sun, Y. (2015). Drought-influenced mortality of tree species with different predawn leaf water dynamics in a decade-long study of a Central US forest. *Biogeosciences*, *12*(10), 2831–2845. <https://doi.org/10.5194/bg-12-2831-2015>

- Gu, L., Pallardy, S. G., Hosman, K. P., & Sun, Y. (2016). Impacts of precipitation variability on plant species and community water stress in a temperate deciduous forest in the Central US. *Agricultural and Forest Meteorology*, *217*, 120–136. <https://doi.org/10.1016/j.agrformet.2015.11.014>
- Gu, L., Pallardy, S. G., Yang, B., Hosman, K. P., Mao, J., Ricciuto, D., et al. (2016). Testing a land model in ecosystem functional space via a comparison of observed and modeled ecosystem flux responses to precipitation regimes and associated stresses in a Central U.S. forest. *Journal of Geophysical Research: Biogeosciences*, *121*, 1884–1902. <https://doi.org/10.1002/2015JG003302>
- Harrison, R. G., & Hanna, E. (2016). The solar eclipse: a natural meteorological experiment. *Philosophical Transactions of the Royal Society A*, *374*(2077), 20150225. <https://doi.org/10.1098/rsta.2015.0225>
- Knapp, A. K. (1993). Gas exchange dynamics in C3 and C4 grasses: Consequence of differences in stomatal conductance. *Ecology*, *74*(1), 113–123. <https://doi.org/10.2307/1939506>
- Kucera, C. L., Dahlman, R. C., & Koelling, M. R. (1965). Total net productivity and turnover on an energy basis for tallgrass prairie. *Ecology*, *48*(4), 536–541.
- Lee, T. R., Buban, M., Palecki, M. A., Leeper, R. D., Diamond, H. J., Dumas, E., et al. (2018). Great American eclipse data may fine-tune weather forecasts. *Eos*, *99*. <https://doi.org/10.1029/2018EO103931>
- Leuning, R. (2004). Measurements of trace gas fluxes in the atmosphere using eddy covariance: WPL corrections revisited. In *Handbook of Micrometeorology* (pp. 119–132). Dordrecht, Netherlands: Kluwer Academic Publishers.
- Leuning, R. (2007). The correct form of the Webb, Pearman and Leuning equation for eddy fluxes of trace gases in steady and non-steady state, horizontally homogeneous flows. *Boundary-Layer Meteorology*, *123*(2), 263–267. <https://doi.org/10.1007/s10546-006-9138-5>
- Mauder, M., Desjardins, R. L., Oncley, S. P., & MacPherson, I. (2007). Atmospheric response to a partial solar eclipse over a cotton field in central California. *Journal of Applied Meteorology and Climatology*, *46*(11), 1792–1803. <https://doi.org/10.1175/2007JAMC1495.1>
- Monteith, J. L., & Unsworth, M. H. (1990). *Principles of Environmental Physics* (1st ed.). London UK: Edward Arnold.
- Pingintha, N., Leclerc, M. Y., Beasley, J. P., Durden, D., Zhang, G., Senthong, C., & Rowland, D. (2010). Hysteresis response of daytime net ecosystem exchange during drought. *Biogeosciences*, *7*(3), 1159–1170. <https://doi.org/10.5194/bg-7-1159-2010>
- Raupach, M. R., & Finnigan, J. J. (1988). “Single-layer models of evaporation from plant canopies are incorrect but useful, whereas multilayer models are correct but useless”: Discuss. *Australian Journal of Plant Physiology*, *15*(6), 705–716. <https://doi.org/10.1071/PP9880705>
- Sadler, E. J., Lerch, R. N., Kitchen, N. R., Anderson, S. H., Baffaut, C., Sudduth, K. A., et al. (2015). Long-term agroecosystem research in the Central Mississippi River Basin: Introduction, establishment, and overview. *Journal of Environmental Quality*, *44*(1), 3–12. <https://doi.org/10.2134/jeq2014.11.0481>
- Schotanus, P., Nieuwstadt, F. T. M., & De Bruin, H. A. R. (1983). Temperature measurement with a sonic anemometer and its application to heat and moisture fluxes. *Boundary-Layer Meteorology*, *26*(1), 81–93. <https://doi.org/10.1007/BF00164332>
- Stewart, R. B., & Rouse, W. R. (1974). Radiation and energy budgets at an arctic site during the solar eclipse of July 10, 1972. *Arctic and Alpine Research*, *6*(2), 231–236. <https://doi.org/10.2307/1550088>
- Torrence, C., & Compo, G. P. (1998). A practical guide to wavelet analysis. *Bulletin of the American Meteorological Society*, *79*(1), 61–78. [https://doi.org/10.1175/1520-0477\(1998\)079<0061:APGTWA>2.0.CO;2](https://doi.org/10.1175/1520-0477(1998)079<0061:APGTWA>2.0.CO;2)
- Turner, D. D., Wulfmeyer, V., Behrendt, A., Bonin, T. A., Choukulkar, A., Newsom, R. K., et al. (2018). Response of the land-atmosphere system over north-central Oklahoma during the 2017 eclipse. *Geophysical Research Letters*, *45*, 1668–1675. <https://doi.org/10.1002/2017GL076908>
- Vico, G., Manzoni, S., Palmroth, S., & Katul, G. (2011). Effects of stomatal delays on the economics of leaf gas exchange under intermittent light regimes. *The New Phytologist*, *192*(3), 640–652. <https://doi.org/10.1111/j.1469-8137.2011.03847.x>
- Webb, E. K., Pearman, G. I., & Leuning, R. (1980). Correction of flux measurements for density effects due to heat and water vapour transfer. *Quarterly Journal of the Royal Meteorological Society*, *106*(447), 85–100. <https://doi.org/10.1002/qj.49710644707>
- Wilczak, J., Oncley, S., & Stage, S. (2001). Sonic anemometer tilt correction algorithms. *Boundary-Layer Meteorology*, *99*(1), 127–150. <https://doi.org/10.1023/A:1018966204465>
- Wood, J. D., Knapp, B. O., Muzika, R.-M., Stambaugh, M. C., & Gu, L. (2018). The importance of drought–pathogen interactions in driving oak mortality events in the Ozark border region. *Environmental Research Letters*, *13*(1), 015004. <https://doi.org/10.1088/1748-9326/aa94fa>
- Xu, K., Metzger, S., & Desai, A. R. (2017). Upscaling tower-observed turbulent exchange at fine spatio-temporal resolution using environmental response functions. *Agricultural and Forest Meteorology*, *232*, 10–22. <https://doi.org/10.1016/j.agrformet.2016.07.019>
- Yang, B., Hanson, P. J., Riggs, J. S., Pallardy, S. G., Heuer, M., Hosman, K. P., et al. (2007). Biases of CO₂ storage in eddy flux measurements in a forest pertinent to vertical configurations of a profile system and CO₂ density averaging. *Journal of Geophysical Research*, *112*, D20123. <https://doi.org/10.1029/2006JD008243>
- Yang, B., Pallardy, S. G., Meyers, T. P., Gu, L. H., Hanson, P. J., Wullschlegel, S. D., et al. (2010). Environmental controls on water use efficiency during severe drought in an Ozark forest in Missouri, USA. *Global Change Biology*, *16*(8), 2252–2271. <https://doi.org/10.1111/j.1365-2486.2009.02138.x>
- Yost, M. A., Kitchen, N. R., Sudduth, K. A., Sadler, E. J., Drummond, S. T., & Volkmann, M. R. (2017). Long-term impact of a precision agriculture system on grain crop production. *Precision Agriculture*, *18*(5), 823–842. <https://doi.org/10.1007/s11119-016-9490-5>
- Zhang, J., Griffis, T. J., & Baker, J. M. (2006). Using continuous stable isotope measurements to partition net ecosystem CO₂ exchange. *Plant, Cell and Environment*, *29*(4), 483–496. <https://doi.org/10.1111/j.1365-3040.2005.01425.x>